

# A Wearable Breath Sensor Based on Fiber-Tip Microcantilever

Cong Zhao <sup>1,2,†</sup> , Dan Liu <sup>1,2,†</sup>, Zhihao Cai <sup>1,2</sup>, Bin Du <sup>1,2</sup>, Mengqiang Zou <sup>1,2</sup>, Shuo Tang <sup>3</sup>, Bozhe Li <sup>1,2</sup>, Cong Xiong <sup>1,2</sup>, Peng Ji <sup>1,2</sup>, Lichao Zhang <sup>1,2</sup> , Yuan Gong <sup>1,2</sup>, Gaixia Xu <sup>3</sup>, Changrui Liao <sup>1,2,\*</sup> and Yiping Wang <sup>1,2</sup> 

- <sup>1</sup> Key Laboratory of Optoelectronic Devices and Systems of Ministry of Education and Guangdong Province, College of Physics and Optoelectronic Engineering, Shenzhen University, Shenzhen 518060, China; zhaocong@szu.edu.cn (C.Z.); 2150120415@email.szu.edu.cn (D.L.); 2060453003@email.szu.edu.cn (Z.C.); dubin2016@email.szu.edu.cn (B.D.); zoumengqiang2020@email.szu.edu.cn (M.Z.); libozhe2019@email.szu.edu.cn (B.L.); xiongcong2018@email.szu.edu.cn (C.X.); jipeng\_2013@163.com (P.J.); lc Zhang5354@szu.edu.cn (L.Z.); ygong@uestc.edu.cn (Y.G.); ypwang@szu.edu.cn (Y.W.)
  - <sup>2</sup> Shenzhen Key Laboratory of Photonic Devices and Sensing Systems for Internet of Things, Guangdong and Hong Kong Joint Research Centre for Optical Fiber Sensors, Shenzhen University, Shenzhen 518060, China
  - <sup>3</sup> Guangdong Key Laboratory for Biomedical Measurements and Ultrasound Imaging, School of Biomedical Engineering, Health Science Center, Shenzhen University, Shenzhen 518055, China; tangshuo2020@email.szu.edu.cn (S.T.); xugaixia@szu.edu.cn (G.X.)
- \* Correspondence: cliao@szu.edu.cn; Tel.: +86-755-2606-6281
- † These authors contributed equally to this work.

**Abstract:** Respiration rate is an essential vital sign that requires monitoring under various conditions, including in strong electromagnetic environments such as in magnetic resonance imaging systems. To provide an electromagnetically-immune breath-sensing system, we propose an all-fiber-optic wearable breath sensor based on a fiber-tip microcantilever. The microcantilever was fabricated on a fiber-tip by two-photon polymerization microfabrication based on femtosecond laser, so that a micro Fabry–Pérot (FP) interferometer was formed between the microcantilever and the end-face of the fiber. The cavity length of the micro FP interferometer was reduced as a result of the bending of the microcantilever induced by breath airflow. The signal of breath rate was rebuilt by detecting power variations of the FP interferometer reflected light and applying dynamic thresholds. The breath sensor achieved a high sensitivity of 0.8 nm/(m/s) by detecting the reflection spectrum upon applied flow velocities from 0.53 to 5.31 m/s. This sensor was also shown to have excellent thermal stability as its cross-sensitivity of airflow with respect to the temperature response was only 0.095 (m/s)/°C. When mounted inside a wearable surgical mask, the sensor demonstrated the capability to detect various breath patterns, including normal, fast, random, and deep breaths. We anticipate the proposed wearable breath sensor could be a useful and reliable tool for respiration rate monitoring.

**Keywords:** Fabry–Pérot interferometer; breath sensor; micro-cantilever; two-photon polymerization; fiber sensor; wearable device



**Citation:** Zhao, C.; Liu, D.; Cai, Z.; Du, B.; Zou, M.; Tang, S.; Li, B.; Xiong, C.; Ji, P.; Zhang, L.; et al. A Wearable Breath Sensor Based on Fiber-Tip Microcantilever. *Biosensors* **2022**, *12*, 168. <https://doi.org/10.3390/bios12030168>

Received: 17 February 2022

Accepted: 3 March 2022

Published: 7 March 2022

**Publisher's Note:** MDPI stays neutral with regard to jurisdictional claims in published maps and institutional affiliations.



**Copyright:** © 2022 by the authors. Licensee MDPI, Basel, Switzerland. This article is an open access article distributed under the terms and conditions of the Creative Commons Attribution (CC BY) license (<https://creativecommons.org/licenses/by/4.0/>).

## 1. Introduction

Respiration rate (RR) is defined as the number of breaths per minute (bpm) and is a clinical sign that represents lung ventilation. RR normally ranges from 12 to 20 bpm for a healthy adult at rest [1]. RR has been determined as the vital sign that is most necessary to be continuously monitored [2]. It can reflect clinical information relating to neurological, cardiac, and pulmonary conditions. According to the guidelines from the National Institute for Health and Care Excellence of the United Kingdom in 2007, RR is the most sensitive parameter to detect any clinical deterioration.

There are various breath sensors for RR measurements, which can generally be classified as contact or noncontact. Contact methods refer to the cases in which the sensing system (or part of it) is directly attached to the subject's body to detect signals including

breath airflow, air temperature, humidity, specific components (e.g., CO<sub>2</sub>), and chest wall movements [3,4]. For noncontact methods, the instrument does not contact the subject, and uses radar, thermal, or optical-imaging-based monitoring solutions [5]. To date, electronic sensors are still the most mainstream of the commercialized breath sensors. However, these sensors are not capable of operating in strong electromagnetic environments due to the electronic transducers inside [6]. In fact, in situations associated with strong electromagnetic environments (e.g., in magnetic resonance imaging (MRI) systems), breath monitoring is still required for various purposes. These purposes include health monitoring, motion compensation, and clinical research such as functional MRI [7].

Fiber-optic sensors are attractive because they are immune to electromagnetic radiation. They also have the intrinsic advantages of flexibility, robustness, fast response, compact size, light weight, and remote sensing capability. Hence, fiber-optic sensors have recently attracted growing attention in applications for breath sensing, especially during MRI examination, as demonstrated in [8–11]. Among these fiber-optic sensors, fiber-optic-based flowmeters are an important category, and their principle of operation is based on the changes of coupled light power with fiber bending (or displacement) caused by the inhaled or exhaled airflow [12–14]. However, these types of sensors have the disadvantage of being sensitive to body motion artifacts, since the body motion of subjects also induces the macro-bending or displacement of fibers [3].

With the development of two-photon polymerization (TPP) microfabrication based on femtosecond (fs) laser, microstructures such as cantilever and clamped-beam can be directly fabricated at the end-face of optical fiber to form a micro Fabry–Pérot (FP) interferometer as a light-coupled microscale sensing platform. TPP microfabrication is a simple direct-writing technology and does not require an additional etching or coating process. Recently, our group demonstrated the applications of a micro FP interferometer on a fiber-tip for the measurement of nanoforce [15] and hydrogen [16] with high sensitivity and rapid response. These relevant works prove that the microcantilever is super sensitive to mechanical loading, with a detection limit down to tens of nanonewtons [15].

In this paper, a breath sensor based on a microcantilever fabricated on a fiber-tip is presented. The fiber-tip microcantilever was directly printed by TPP microfabrication, hence forming a micro FP interferometer. The RR signal was detected by demodulating the FP interferometer cavity length change induced by the bending of the microcantilever under the exhalation airflow, as shown in Figure 1. The airflow responses and temperature stability of the breath sensor were investigated. The real-time RR monitoring of different breath patterns was also demonstrated to prove the industrial applicability of the device.

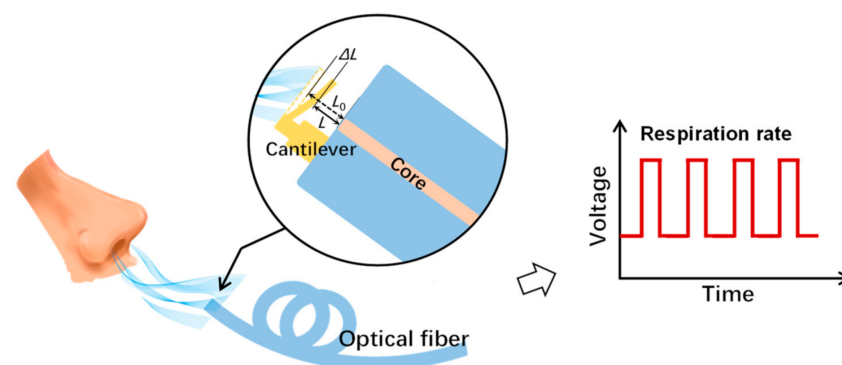


**Figure 1.** Schematic diagram of the proposed breath sensor. During the inhalation and exhalation cycles, the fiber-tip microcantilever deflects and recovers repeatedly. Thus, the respiration rate can be measured by recording the amplitude changes of the reflected light from the micro Fabry–Pérot interferometer formed by the microcantilever and the fiber end-face.

## 2. Materials and Methods

### 2.1. Device Fabrication

A commercial negative photoresist (PR) (Zhichu Optics Co., Ltd., Shenzhen, China) was applied for fabricating the fiber-tip microcantilever. The PR was composed of a photo-initiator (IGR-369, from Ciba Specialty Chemicals, Basel, Switzerland), monomers (SR444, SR368 and SR454, from Sartomer, Exton, PA, USA), a polymerization inhibitor (4-hydroxyanisole, MEHQ, from Sigma Aldrich, St. Louis, MO, USA), and an accelerator promoter (tetraethyl thiuram disulphide, TED, from Sigma Aldrich, St. Louis, MO, USA). The fabrication process has been described in detail elsewhere [15–17]. Briefly, a fiber-tip microcantilever was fabricated by TPP microfabrication based on femtosecond laser as shown in Figure 2A. Firstly, a precleaned single-mode fiber (SMF) was mounted in between a glass slide and a coverslip with its end-face immersed in a PR droplet. The polymerization of the microcantilever was then performed on a 3D air-bearing stage (Aerotech, Pittsburgh, PA, USA). The key parameters of the fs laser used in polymerization included a pulse width of 250 fs, a central wavelength of 1026 nm, and a pulse repetition rate of 200 kHz. To speed up the polymerization, the laser power was determined as 2 mW and the scanning velocity was determined as 300  $\mu\text{m/s}$ . After polymerization, the unpolymerized PR was washed away by a developer of acetone and isopropyl alcohol (1:4,  $v/v$ ). After washing and drying, the fiber-tip microcantilever was eventually fabricated. As shown in Figure 2B,C, the geometric parameters of the microcantilever were designed to be a length of 30  $\mu\text{m}$ , a width of 20  $\mu\text{m}$ , and a thickness of 2  $\mu\text{m}$ . The cavity length of the fiber-tip FP interferometer was designed as 50  $\mu\text{m}$ .

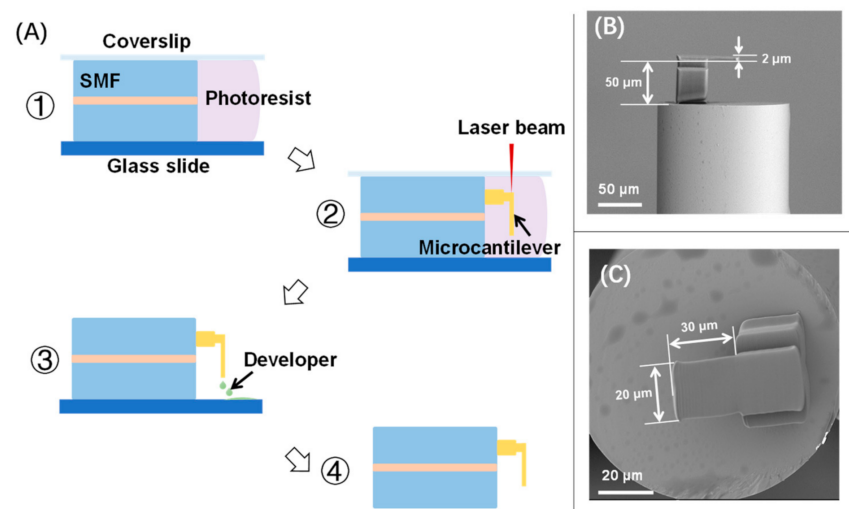


**Figure 2.** (A) Microfabrication process of a fiber-tip microcantilever by TPP technology based on fs laser; (B,C) are representative scanning electron microscopy (SEM) images of the fabricated device.

### 2.2. Reflection Spectrum Measurement

The reflection spectrum from the micro FP interferometer formed by the fiber-tip microcantilever and the fiber end-face was measured using the setups shown in Figure 3A. An ASE (amplified spontaneous emission) light source (1250–1650 nm, Fiber Lake Co., Ltd., Shenzhen, China) was used to generate the input light of the micro FP interferometer, where a three-beam interference occurred with lights from the fiber-tip and the top and bottom surfaces of the microcantilever [16]. The following equation describes the function between the shift of dip wavelength ( $\Delta\lambda_r$ ) and the cavity length reduction ( $\Delta L$ ) of the micro FP interferometer

$$\Delta\lambda_r/\lambda_r = \Delta L/L \quad (1)$$

where  $\lambda_r$  is the dip wavelength and  $L$  is the cavity length. An optical spectrum analyzer (AQ6317C, Yokogawa, Tokyo, Japan) was utilized to record the reflection spectrum signal.

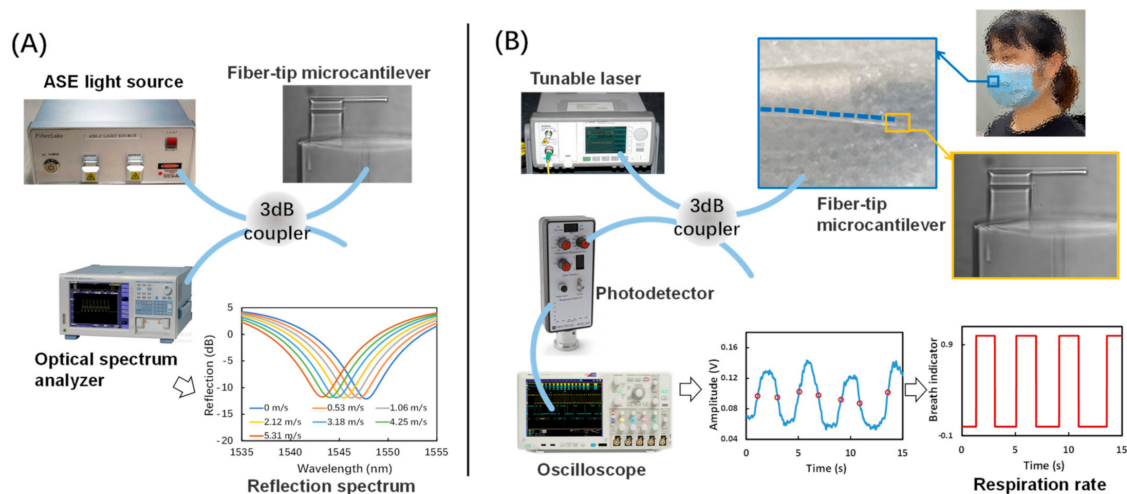


**Figure 3.** The experimental setups for (A) reflection spectrum measurement and (B) breath sensing.

### 2.3. Breath Sensing

The setup of breath sensing by measuring the RR is shown in Figure 3B. The intensity of the light reflected from the micro FP interferometer was monitored. The amplitude of this signal is a function of the FP interferometer cavity length  $L$  [18]. In this setup, input light from a tunable laser source (N7776C and N7778C, Keysight, Santa Rosa, CA, USA) was coupled to the micro FP interferometer through a 3 dB coupler. The wavelength of the input light was identified as corresponding to the  $-3$  dB value upon the peak of reflection spectrum ( $\sim 1545$  nm). The intensity of reflected light was then converted into an electric power signal and recorded by an oscilloscope (MDO3000, Tektronix, Beaverton, OR, USA). Due to its microscale size and excellent flexibility, the proposed breath sensor was able to be attached inside a disposable surgical mask, which was worn by the subject during the breath testing. Thus, when the subject breathed against the microcantilever, the corresponding RR signal could be collected from the oscilloscope and further processed by a dynamic-thresholding algorithm to generate the breath pattern.

## 3. Results and Discussion

### 3.1. Airflow Response

To measure the airflow response, the sensor was mounted in a silicone tube (3 mm in diameter), which was connected to a mass flow controller (MFC, Beijing Sevenstar Flow Co., Ltd., Beijing, China) controlling the dried nitrogen flow at a series of flow velocities from 0.53 to 5.31 m/s. This testing range covered the normal flow velocity of human breath of around 2 m/s [19,20]. Each flow velocity was applied for at least 5 min to ensure that the response of the breath sensor became stable. The evolution of the reflection spectrum as a function of applied airflow velocity was recorded. As shown in Figure 4A, the dip wavelength ( $\sim 1545$  nm) of the reflection spectrum showed a blue shift ( $\sim 5$  nm) with increasing flow velocity. This could be induced by the decrease of the interferometer cavity length due to bending of microcantilever under the aerodynamic loading. Figure 4B illustrates the linear fitting of the dip wavelength as a function of flow velocity, with a sensitivity of 0.8 nm/(m/s).

To mimic the periodic airflow of human breath, the MFC was also used to generate airflow pulses at a frequency of 15 times/min, which is within the normal range of respiration rate (12 to 20 bpm). In each airflow pulse cycle of  $\sim 4$  s, the MFC was first closed for  $\sim 2$  s, and then opened to generate airflow for  $\sim 2$  s at preset flow velocities from 1.06 to 5.31 m/s. The amplitude of the reflected light from the micro FP interferometer was then recorded, as shown in Figure 5. Figure 5A shows the voltage of the amplitude signal as a function of the flow velocities of applied airflow pulses. As the flow velocity first increased and then decreased, the output voltage value also increased and then decreased with almost the same frequency



of input airflow pulses. This change was also due to the decrease of interferometer cavity length induced by the bending of the microcantilever under the aerodynamic loading. It was also noted that, due to the momentum of the microcantilever motion, there was a backward voltage when the microcantilever recovered from the aerodynamic-loading-induced bending, especially in the cases of larger flow velocities. Figure 5B plots the output voltage value as a function of the input flow velocity, with a linear fitting result showing a slope of 93 mV/(m/s). From the data in Figure 5B, a hysteresis error of less than 5% was calculated. Figure 5C shows a representative response under an airflow pulse, with a typical response and recovery time of  $\sim 300$  ms and  $\sim 500$  ms, respectively.

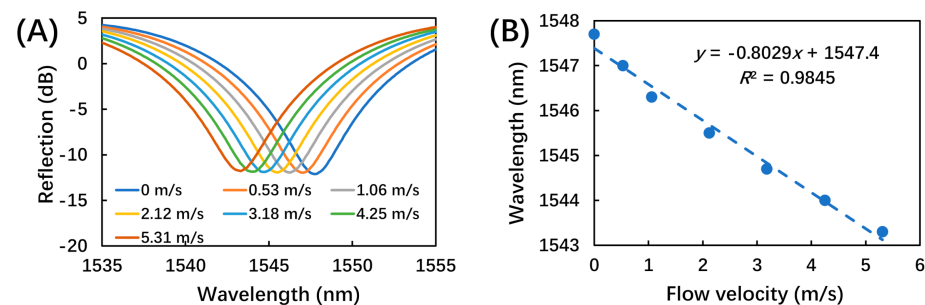


**Figure 4.** The responses of the breath sensor upon airflows at different flow velocities. (A) Reflection spectrum as a function of wavelength at different flow velocities; (B) linear fitting of the dip wavelength ( $\sim 1545$  nm) as a function of flow velocity.

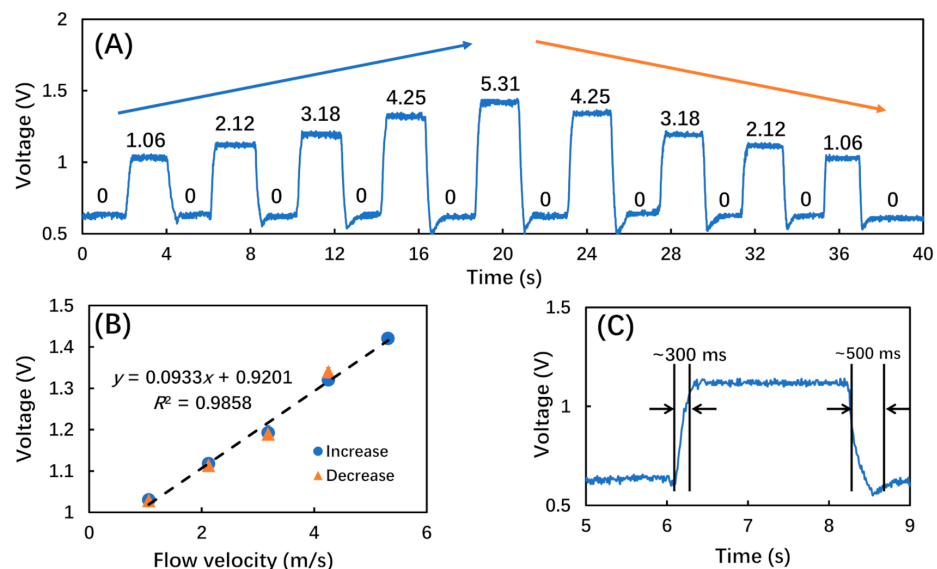


**Figure 5.** The responses of the breath sensor under airflow pulses at different flow velocities. (A) The amplitude of the reflected light under airflow pulses at different flow velocities (marked above the corresponding voltage data curves, unit: m/s); (B) linear fitting of output voltage data as a function of flow velocity; (C) a zoomed-in representative response under an airflow pulse of 2.12 m/s.

### 3.2. Temperature Stability

Considering the low melting point of the photoresist and the normal operation conditions of the breath sensor, the temperature response was tested from 25 to 55 °C. The sensor was placed in an oven with well-controlled temperature and the temperature was increased in steps of 5 °C in the tested range. Each temperature was maintained for 15 min to allow the sensor to reach a stable output. Then, both the evolution of reflection spectrum and the amplitude signal were recorded.

As shown in Figure 6A, the dip wavelength ( $\sim 1545$  nm) of the reflection spectrum exhibited a red shift ( $\sim 2$  nm) with increasing temperature. This was induced by the increase

of the interferometer cavity length due to the heat-induced swelling of the photoresist [16]. Figure 6B illustrates the linear fitting of the dip wavelength as a function of temperature, with a sensitivity of 76.1 pm/°C. The cross-sensitivity of airflow with respect to temperature was calculated to be 0.095 (m/s)/°C, as the ratio of the two corresponding sensitivities shown in Figures 5B and 6B.

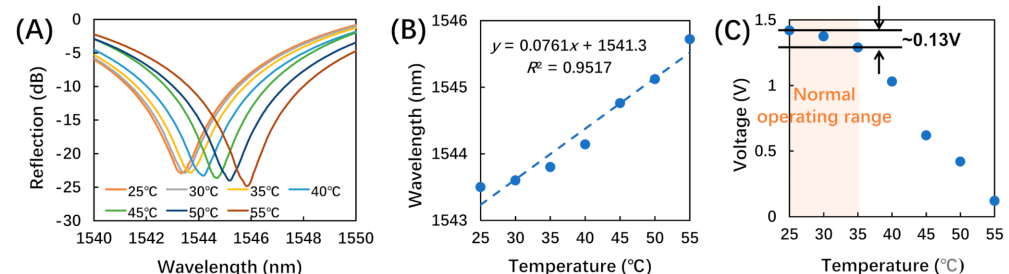


**Figure 6.** The temperature responses of the breath sensor. (A) Reflection spectra at different temperatures; (B) linear fitting of the dip wavelength ( $\sim 1545$  nm) as a function of temperature; (C) amplitude of the reflected light under normal operating temperatures.

Figure 6C shows the amplitude of the reflected light as a function of temperature. As a prototype demonstration, we constrained the application of the proposed breath sensor to be for indoor use at a room temperature of around 25 °C. Considering that body temperature is 37 °C, we determined the normal operation temperature as 25 to 35 °C [21]. Within this range, the output voltage only increased by 0.13 V as shown in Figure 6C, which was only  $\sim 10.8\%$  of the typical airflow response ( $\sim 1.2$  V) to the flow rate of 2.12 m/s (the typical flow rate of human breath [19,20]). As a result, the impact of temperature variation under normal operating conditions was insignificant. Thus, both the low cross-sensitivity and the voltage change under normal operating temperatures indicate that the breath sensor has relatively low sensitivity to ambient temperature changes under normal operating conditions. However, there are many locations and situations with higher or lower temperatures, especially in outdoor settings, which would influence the performance of the proposed breath sensor. Thus, future work to design and fabricate proper packaging for the breath sensor is needed to minimize the impacts from ambient temperature change.

### 3.3. Breath Sensing

The breath sensor was mounted in a disposable surgical mask to monitor human respiration, as shown in Figure 3B. During the testing, the subject was required to perform each of the breath patterns, including regular breath, deep breath, fast breath, and random breath. The corresponding time-dependent amplitude of the reflected light was recorded and processed by the dynamic thresholding algorithm to rebuild the breath pattern.

Figure 7A shows the recorded amplitude signal of a regular breath lasting 100 s. During the exhale cycle, the breath from the subject's nose induced a deflection in the fiber-tip microcantilever, which altered the amplitude signal. After it was converted to a voltage signal by the photodetector, the amplitude signal could be used to identify the inhalation and exhalation states. The baseline and amplitude signal showed certain fluctuations due to the turbulent flow within the space between the mask and the subject's face, and the incomplete recovery of the fiber-tip microcantilever. Thus, a uniform threshold was not applicable for determining the inhalation and exhalation states.

Instead, a dynamic threshold was applied to determine the inhalation and exhalation states [12,22,23]. Firstly, the “findpeaks” function in Matlab r2010b (MathWorks, Natick, MA, USA) was utilized to detect the peaks and valleys in the signal of time-dependent amplitude of the reflected light. There were multiple peaks in some of the signals, such as irregular breaths and deep breaths, as shown in Figure 8C,E. In the case of multiple peaks, we used the averaged values of the multiple adjacent peaks to represent the peak value. Secondly, we grouped each adjacent peak and valley as one pair to generate the

threshold. Thirdly, the average values of all the adjacent peak–valley pairs were calculated as the dynamic thresholds, which were eventually used to determine the breath cycles, as shown in Figure 7A marked by empty red circles.

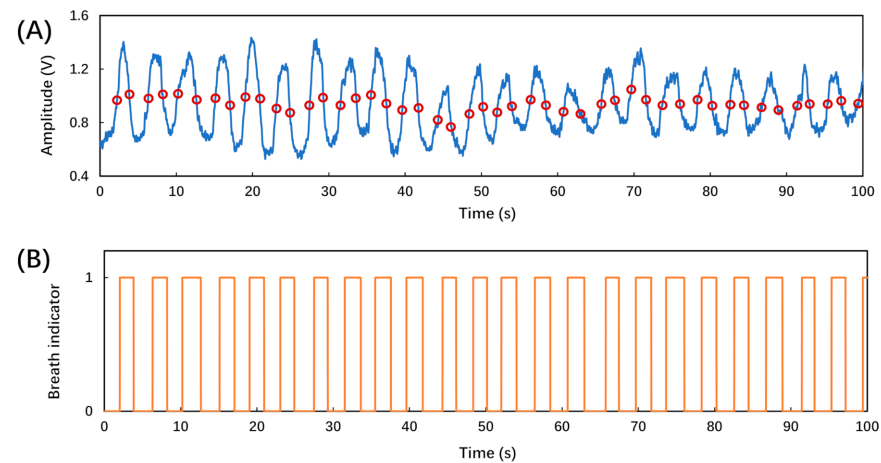


**Figure 7.** (A) Experimentally recorded breathing pattern using the breath sensor, in which the blue curve represents the time-dependent amplitude of the reflected light, and the empty red circles represent the dynamic thresholds in real time; (B) output of the breath analysis program using the dynamic thresholds corresponding to a regular breathing pattern.

Figure 7B shows the breath indicator which reflects the breath cycles of inhalation and exhalation states according to the dynamic thresholds in Figure 7A. The breath indicator was determined as ‘0’ for amplitudes smaller than the dynamic threshold, which represented the inhalation state. On the other hand, the breath indicator was determined as ‘1’ for amplitudes larger than the dynamic threshold, which represented the exhalation state. As shown in Figure 7B, it is clear that the fiber-tip microcantilever-based breath sensor can be applied for monitoring regular breathing.

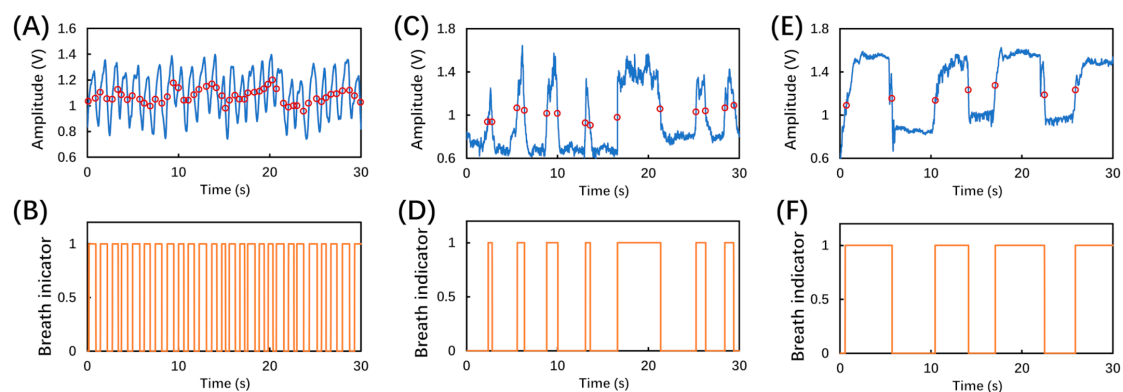


**Figure 8.** Experimentally recorded different breathing patterns and corresponding dynamic thresholds in real time for (A) fast breath, (C) irregular breath, and (E) deep breath; the output of breath analysis program using the dynamic thresholds corresponding to (B) fast breath, (D) irregular breath, and (F) deep breath patterns.

Additionally, in order to demonstrate that the sensor was also capable of monitoring the RR of various breath patterns, three more breathing behaviors were tested and recorded as shown in Figure 8. Figure 8A,C,E shows the recorded amplitude signals lasting 30 s of a fast, irregular, and deep breath, respectively, in which the empty red circles represent the dynamic thresholds in real time. Figure 8B,D,F shows the corresponding breathing patterns using the dynamic thresholds regarding fast, irregular, and deep breaths, respectively.

Thus, the breath sensor was determined to also be capable of monitoring different types of breathing conditions.

During the tests, there were some incorrectly identified respiration signals, which were probably caused by the nonuniform airflow inside the disposable surgical mask. As the breath sensor was mounted inside the mask where the breath airflow was not well controlled, any factors that impact the breath airflow inside the mask would eventually impact the breath-sensing performance. To achieve more uniform breath airflow and reliable breath sensing, the breath sensor could further be integrated into breathing tubes, since these commercialized breathing tubes have a regular geometry and are capable of controlling the airflow direction. In addition, as an all-fiber device, the breath sensor is not only compact but also highly flexible and able to be integrated into oxygen masks, breathing tubes, etc. Due to its miniaturized size and high biocompatibility, it can even be placed close to the nose or lips with negligible discomfort and risks [3].

#### 4. Conclusions

Here we proposed and experimentally demonstrated a novel wearable all-fiber breath sensor, which demonstrated excellent performance for monitoring human breath with different patterns. The sensing mechanism is based on the cavity-length reduction of a micro FP interferometer comprising a fiber-tip microcantilever and the end-face of a fiber, where the length reduction is caused by the mechanical bending of the cantilever under the exhaled airflow. Within the tested flow velocities from 0.53 to 5.31 m/s, the sensor achieved a high sensitivity of 0.8 nm/(m/s) and low cross-sensitivity of airflow with respect to the temperature response, of 0.095 (m/s)/°C. The proposed breath sensor also demonstrated an excellent capability for breath-pattern sensing by applying dynamic thresholds. Thus, the proposed sensor is thermally stable, compact, flexible, and wearable. We believe that it could be a promising key component of wearable RR monitoring devices, especially when using healthcare equipment associated with strong electromagnetic environments.

**Author Contributions:** Conceptualization, C.Z. and C.L.; methodology, D.L.; software, Z.C.; validation, D.L., B.D., S.T., B.L., C.X., P.J., Y.G. and M.Z.; writing—original draft preparation, C.Z.; writing—review and editing, D.L., L.Z. and G.X.; supervision, Y.W. All authors have read and agreed to the published version of the manuscript.

**Funding:** This research was funded by the National Natural Science Foundation of China (NSFC) (62122057, 62075136 and 62101353); Natural Science Foundation of Guangdong Province (2018B030306003 and 2020A0505100066); and the Science and Technology Innovation Commission of Shenzhen (JCYJ20190808162603577 and JCYJ20190808161019406).

**Institutional Review Board Statement:** Ethical review and approval were waived for this study, since the experiments are almost completely safe, do not cause harm to the subject, and do not involve privacy and moral issues.

**Informed Consent Statement:** Written informed consent has been obtained from the subject to publish this paper.

**Data Availability Statement:** The experimental data is contained within the article.

**Conflicts of Interest:** The authors declare no conflict of interest.

#### References

1. Cretikos, M.A.; Bellomo, R.; Hillman, K.; Chen, J.; Finfer, S.; Flabouris, A. Respiratory rate: The neglected vital sign. *Med. J. Aust.* **2008**, *188*, 657–659. [[CrossRef](#)]
2. Marjanovic, N.; Mimos, O.; Guenezan, J. An easy and accurate respiratory rate monitor is necessary. *J. Clin. Monit. Comput.* **2020**, *34*, 221–222. [[CrossRef](#)]
3. Massaroni, C.; Nicolò, A.; Lo Presti, D.; Sacchetti, M.; Silvestri, S.; Schena, E. Contact-based methods for measuring respiratory rate. *Sensors* **2019**, *19*, 908. [[CrossRef](#)] [[PubMed](#)]
4. Folke, M.; Cernerud, L.; Ekström, M.; Hök, B. Critical review of non-invasive respiratory monitoring in medical care. *Med. Biol. Eng. Comput.* **2003**, *41*, 377–383. [[CrossRef](#)] [[PubMed](#)]

5. AL-Khalidi, F.Q.; Saatchi, R.; Burke, D.; Elphick, H.; Tan, S. Respiration rate monitoring methods: A review. *Pediatr. Pulmonol.* **2011**, *46*, 523–529. [[CrossRef](#)] [[PubMed](#)]
6. Dziuda, Ł. Fiber-optic sensors for monitoring patient physiological parameters: A review of applicable technologies and relevance to use during magnetic resonance imaging procedures. *J. Biomed. Opt.* **2015**, *20*, 010901. [[CrossRef](#)] [[PubMed](#)]
7. Urback, A.L.; MacIntosh, B.J.; Goldstein, B.I. Cerebrovascular reactivity measured by functional magnetic resonance imaging during breath-hold challenge: A systematic review. *Neurosci. Biobehav. Rev.* **2017**, *79*, 27–47. [[CrossRef](#)]
8. Dziuda, Ł.; Zieliński, P.; Baran, P.; Krej, M.; Kopka, L. A study of the relationship between the level of anxiety declared by MRI patients in the STAI questionnaire and their respiratory rate acquired by a fibre-optic sensor system. *Sci. Rep.* **2019**, *9*, 4341. [[CrossRef](#)]
9. Yoo, W.-J.; Jang, K.-W.; Seo, J.-K.; Heo, J.-Y.; Moon, J.-S.; Park, J.-Y.; Lee, B.-S. Development of respiration sensors using plastic optical fiber for respiratory monitoring inside MRI system. *J. Opt. Soc. Korea* **2010**, *14*, 235–239. [[CrossRef](#)]
10. Nedoma, J.; Fajkus, M.; Novak, M.; Strbikova, N.; Vasinek, V.; Nazeran, H.; Vanus, J.; Perecar, F.; Martinek, R. Validation of a novel fiber-optic sensor system for monitoring cardiorespiratory activities during MRI examinations. *Adv. Electr. Electron. Eng.* **2017**, *15*, 536–543. [[CrossRef](#)]
11. Lau, D.; Chen, Z.; Teo, J.T.; Ng, S.H.; Rumpel, H.; Lian, Y.; Yang, H.; Kei, P.L. Intensity-modulated microbend fiber optic sensor for respiratory monitoring and gating during MRI. *IEEE Trans. Biomed. Eng.* **2013**, *60*, 2655–2662. [[CrossRef](#)] [[PubMed](#)]
12. Li, X.; Liu, D.; Kumar, R.; Ng, W.P.; Fu, Y.-Q.; Yuan, J.; Yu, C.; Wu, Y.; Zhou, G.; Farrell, G.; et al. A simple optical fiber interferometer based breathing sensor. *Meas. Sci. Technol.* **2017**, *28*, 035105. [[CrossRef](#)]
13. Schena, E.; Saccomandi, P.; Silvestri, S. A high sensitivity fiber optic macro-bend based gas flow rate transducer for low flow rates: Theory, working principle, and static calibration. *Rev. Sci. Instrum.* **2013**, *84*, 024301. [[CrossRef](#)] [[PubMed](#)]
14. Mohanty, L.; Kuang, K.S.C. A breathing rate sensor with plastic optical fiber. *Appl. Phys. Lett.* **2010**, *97*, 073703. [[CrossRef](#)]
15. Zou, M.; Liao, C.; Liu, S.; Xiong, C.; Zhao, C.; Zhao, J.; Gan, Z.; Chen, Y.; Yang, K.; Liu, D.; et al. Fiber-tip polymer clamped-beam probe for high-sensitivity nanoforce measurements. *Light Sci. Appl.* **2021**, *10*, 171. [[CrossRef](#)]
16. Xiong, C.; Zhou, J.; Liao, C.; Zhu, M.; Wang, Y.; Liu, S.; Li, C.; Zhang, Y.; Zhao, Y.; Gan, Z.; et al. Fiber-tip polymer microcantilever for fast and highly sensitive hydrogen measurement. *ACS Appl. Mater. Interfaces* **2020**, *12*, 33163–33172. [[CrossRef](#)]
17. Li, C.; Liao, C.; Wang, J.; Gan, Z.; Wang, Y. Femtosecond laser microprinting of a polymer optical fiber interferometer for high-sensitivity temperature measurement. *Polymers* **2018**, *10*, 1192. [[CrossRef](#)]
18. Iannuzzi, D.; Deladi, S.; Gadgil, V.J.; Sanders, R.G.P.; Schreuders, H.; Elwenspoek, M.C. Monolithic fiber-top sensor for critical environments and standard applications. *Appl. Phys. Lett.* **2006**, *88*, 053501. [[CrossRef](#)]
19. Gupta, J.K.; Lin, C.-H.; Chen, Q. Characterizing exhaled airflow from breathing and talking. *Indoor Air* **2010**, *20*, 31–39. [[CrossRef](#)]
20. Rahimi-Gorji, M.; Pourmehran, O.; Gorji-Bandpy, M.; Gorji, T.B. CFD simulation of airflow behavior and particle transport and deposition in different breathing conditions through the realistic model of human airways. *J. Mol. Liq.* **2015**, *209*, 121–133. [[CrossRef](#)]
21. Popov, T.A.; Kralimarkova, T.Z.; Dimitrov, V.D. Measurement of exhaled breath temperature in science and clinical practice. *Breathe* **2012**, *8*, 186. [[CrossRef](#)]
22. Bertoni, M.; Telias, I.; Urner, M.; Long, M.; Del Sorbo, L.; Fan, E.; Sinderby, C.; Beck, J.; Liu, L.; Qiu, H.; et al. A novel non-invasive method to detect excessively high respiratory effort and dynamic transpulmonary driving pressure during mechanical ventilation. *Crit. Care* **2019**, *23*, 346. [[CrossRef](#)] [[PubMed](#)]
23. Kim, J.; ElMoaqet, H.; Tilbury, D.M.; Ramachandran, S.K.; Penzel, T. Time domain characterization for sleep apnea in oronasal airflow signal: A dynamic threshold classification approach. *Physiol. Meas.* **2019**, *40*, 054007. [[CrossRef](#)] [[PubMed](#)]